Monthly Notices
of the
ROYAL ASTRONOMICAL SOCIETY

MNRAS **463,** 2202–2209 (2016)
Advance Access publication 2016 August 19

doi:10.1093/mnras/stw2065

A LOFAR mini-survey for low-frequency radio emission from the nearest brown dwarfs

Ben Burningham,[1,2★] M. Hardcastle,[2] J. D. Nichols,[3] S. L. Casewell,[3] S. P. Littlefair,[4] C. Stark,[5] M. R. Burleigh,[3] S. Metchev,[6,7] M. E. Tannock,[6] R. J. van Weeren,[8] W. L. Williams[2] and G. A. Wynn[3]

[1]*NASA Ames Research Center, Mail Stop 245-3, Moffett Field, CA 94035, USA*
[2]*Centre for Astrophysics Research, School of Physics, Astronomy and Mathematics, University of Hertfordshire, Hatfield AL10 9AB, UK*
[3]*Department of Physics and Astronomy, University of Leicester, Leicester LE1 7RH, UK*
[4]*Department of Physics and Astronomy, University of Sheffield, Sheffield S3 7RH, UK*
[5]*Division of Computing and Mathematics, Kydd Building, Abertay University, Dundee DD1 1HG, UK*
[6]*Centre for Planetary Science and Exploration, Department of Physics & Astronomy, The University of Western Ontario, London, ON N6A 3K7, Canada*
[7]*Department of Physics & Astronomy, Stony Brook University, Stony Brook, NY 11794-3800, USA*
[8]*Harvard–Smithsonian Center for Astrophysics, 60 Garden Street, Cambridge, MA 02138, USA*

Accepted 2016 August 12. Received 2016 August 12; in original form 2016 May 19

ABSTRACT

We have conducted a mini-survey for low-frequency radio emission from some of the closest brown dwarfs to the Sun with rapid rotation rates: SIMP J013656.5+093347, WISEPC J150649.97+702736.0 and WISEPA J174124.26+255319.5. We have placed robust 3σ upper limits on the flux density in the 111–169 MHz frequency range for these targets: WISE 1506: <0.72 mJy; WISE 1741: <0.87 mJy; SIMP 0136: <0.66 mJy. At 8 h of integration per target to achieve these limits, we find that systematic and detailed study of this class of object at LOFAR frequencies will require a substantial dedication of resources.

Key words: surveys – brown dwarfs – stars: low-mass.

1 INTRODUCTION

With effective temperatures ranging from 2400 K to below 400 K, the atmospheres of ultracool dwarfs (UCDs) link the stellar and planetary regimes. The warmest UCDs extend the cool stellar sequence from the spectral type M7 to the L spectral class ($2400 > T_{\rm eff} > 1400$ K), incorporating objects of both stellar and substellar masses, and displaying optical and infrared spectral morphologies shaped by the development of thick silicate condensate clouds (e.g. Kirkpatrick et al. 1999). At cooler temperatures ($1400 > T_{\rm eff} > 300$ K), T and Y dwarfs are exclusively substellar, with the spectral sequence defined by the development of broad absorption bands due to water, methane and ammonia (e.g. Burgasser et al. 2006; Cushing et al. 2011; Canty et al. 2015; Line et al. 2015). The defining feature of brown dwarfs is their failure to reach the main sequence, meaning that they cool and fade as they age. As a result, brown dwarfs of planetary mass (a few $M_{\rm Jupiter}$) have been found across the L, T and Y dwarf spectral classes at a variety of ages and temperatures (e.g. Burgasser et al. 2010; Burningham et al. 2011; Cushing et al. 2011; Delorme et al. 2013; Faherty et al. 2013; Liu et al. 2013; Naud et al. 2014). Spanning this transitionary parameter space, substellar UCDs represent outstanding opportunities for understanding the physics, chemistry and dynamics that differentiate the stellar and planetary domains. This is particularly true for understanding magnetic fields and their interaction with atmospheres and space environments.

Fully convective early-type M dwarfs display well-documented evidence of stellar magnetic activity in the form of flares, and correlated X-ray, Hα and radio emission. However, the fraction of total luminosity emitted via optical and X-ray tracers of activity drops off rapidly in the UCD regime as atmospheric ion fractions drop with decreasing temperature, and as the increasingly neutral atmospheres decouple from magnetic fields (Gizis et al. 2000; Mohanty et al. 2002). Surprisingly, radio luminosity does not drop off, thereby violating the correlation between radio and X-ray flux typically seen in stellar sources (Gudel et al. 1993; Benz & Guedel 1994). This fact, and the observed brightness temperatures of the radio emission, suggests that despite the cool temperatures, a significant source of plasma exists in the envelope surrounding the UCD radio sources. Radio emission has been detected in ≈5–10 per cent of UCDs across spectral types ranging from M9 to T6, spanning a $T_{\rm eff}$ range of some 1500 K, incorporating largely neutral photospheres (e.g. Berger et al. 2001; Berger 2006; McLean, Berger & Reiners 2012; Route & Wolszczan 2012; Williams, Berger & Zauderer 2013; Kao et al. 2016; Lynch et al. 2016), although the majority

★ E-mail: b.burningham@herts.ac.uk

of these have earlier spectral types. Indeed, until the survey of Kao et al. (2016), over 60 objects with spectral types later than L6 had been surveyed, but only one has been detected to be radio emitting (Antonova et al. 2013; Route & Wolszczan 2013). Characterizing this new population of radio emitters is now the target of significant enquiry (e.g. McLean et al. 2012; Williams et al. 2013; Kao et al. 2016).

Pulsed periodic and quiescent emission has been detected from the currently identified radio 'active' UCDs via a number of studies in the 8.5 and 4.9 GHz radio bands (e.g. Hallinan et al. 2006, 2007, 2008; Berger et al. 2009; Williams, Cook & Berger 2014). The periodic pulses are coherent, apparently rotationally modulated and typically display 100 per cent polarization. They have been attributed to the electron cyclotron maser instability (ECMI; e.g. Treumann 2006; Hallinan et al. 2008). Quiescent emission has been detected in all cases where pulsed emission is present, and is essentially unpolarized. It has been explained as either a component of the ECMI emission that has been depolarized during transmission through the UCD's magnetosphere (Hallinan et al. 2008) or as gyrosynchrotron emission (Berger 2002). Gyrosynchrotron emission has been suggested as the cause of non-flaring emission detected in a UCD (TVLM513-46546) at 95 GHz with the Atacama Large Millimeter Array (Williams et al. 2015). This object also emits via the ECMI mechanism (which could not produce 95 GHz emission for plausible field strengths), emitting periodic pulses on its rotation period. Ravi et al. (2011) also suggest that gyrosynchrotron emission is responsible for non-flaring 4.5–24 GHz radio emission detected from DENIS-P J104814.9−395604. TVLM513-46546 was also observed at 325 MHz without detection at the 0.8 mJy level by Jaeger et al. (2011).

The ECMI mechanism is responsible for radio emission across a variety of astronomical contexts, from Solar system planets to emission from some types of solar flare through to massive star radio emission (Treumann 2006). ECMI emission is inherently variable, and produces directional (beamed) circularly or elliptically polarized emission, consistent with the rotationally modulated pulses seen in UCDs. Recently, Nichols et al. (2012) have modelled the ECMI emission from UCDs as originating from the upward magnetic field-aligned component of a large-scale magnetosphere–ionosphere coupling current system flowing as a result of a meridional angular velocity gradient in ionospheric plasma. The Nichols et al. (2012) model broadly matches the properties of the emission seen in the UCDs to which it has been applied. Furthermore, the wavelength dependence of the optical variability of radio-emitting UCDs has been interpreted as arising as a result of non-thermal ionization caused when the electron currents impact the photosphere (Hallinan et al. 2015). Thus, the optical and radio emission can be seen as evidence for powerful auroral currents in UCDs, similar to e.g. Jupiter's main auroral oval (Grodent et al. 2003) and significant components of its decametric, hectometric and kilometric radio bursts (Zarka 1998).

At Jupiter, the flow shear is a result of centrifugally driven outward diffusion of plasma generated at the volcanic moon Io, which orbits deep within the rapidly rotating Jovian magnetosphere (Hill 1979; Cowley & Bunce 2001; Nichols & Cowley 2003, 2004, 2005). Conservation of angular momentum results in a gradient in the angular velocity with radial distance, which, when mapped along magnetic field lines to the planet, results in a meridional current flowing in the Pedersen conducting layer of the atmosphere (i.e. where the collisional frequency is comparable to the gyrofrequency, allowing maximum ion mobility in the direction of the electric field). From current continuity, the divergence of the Pedersen current yields the field-aligned current, the upward component of which (corresponding to downward-precipitating electrons) gives rise to the auroral and radio emissions. Nichols et al. (2012) hypothesized that either such centrifugally driven outflow or the interaction of the rotating magnetosphere with an external flowing medium (Isbell, Dessler & Waite 1984) could produce an angular velocity gradient at brown dwarfs. Regardless of the ultimate cause of the flow shear, however, the expected radio spectrum is essentially flat, with a high-frequency cut-off set by the cyclotron frequency $\nu = eB_i/2\pi m_e$ (where B_i is the polar magnetospheric magnetic field strength) at the top of the ionosphere and a low frequency cut-off given by the cyclotron frequency at the altitude of the field-aligned voltage that drives the upward field-aligned current. The radio luminosity is principally dependent on the dwarf's angular velocity, magnetic field strength, ionospheric Pedersen conductance and the properties of the high-latitude plasma, so its measurement provides the opportunity to study the plasma environment of brown dwarfs and identify departures and similarities to Jovian case, such as (for example) the presence or absence of an Io-analogue companion.

Despite the progress made in the field, a number of problems remain for understanding the radio properties of the wider population. Most pressing is identifying which properties distinguish the radio 'active' objects from the 'inactive' ones. Overall, about 5 per cent of UCDs have been detected at GHz bands, and the hit rate is biased towards types earlier than L3.5, for which the detection rate is ∼10 per cent compared with ∼2 per cent for types later than L3.5 (Antonova et al. 2013).

Several explanations could explain this low rate of detection. First, the electrodynamic engine responsible for the radio emission may be absent or too weak to power detectable emission in the majority of cases. If the electrodynamic engine is corotation breakdown as in the case of the Jovian main auroral oval and the Nichols et al. (2012) model, then this may indicate e.g. a lack of plasma sources, small ionospheric Pedersen conductance or insufficient velocity shear. Similarly, if the engine is the interaction between the UCD magnetic field and orbiting planets, then the low detection may simply indicate the rarity of such systems.

Another possibility is that geometric effects might hide radio emitters, since the beaming of the ECMI generated emission can be expected to restrict the visibility to only favourable geometries. However, the low detection rates would require a much tighter typical beam than is seen for Jupiter's auroral radio emission (≈1.6 sr), which would give rise to an expected detection rate of about 46 per cent in the absence of other factors. The pulse duty cycles, which range from 0.05 to 0.3, also suggest that beaming is unlikely to account for the low detection rate. This is further supported by the results of Pineda et al. (2016), who find that the Hα detection rate in this regime is similar to the radio detection rate. The dichotomy in detection rates between objects earlier than L3.5 and later types further suggests that geometry is not the dominant factor. In addition, the quiescent emission is often only a factor of a few fainter than the pulses (e.g. Hallinan et al. 2008), and it should be unaffected by viewing angle.

The remaining likely cause for the low detection rate is the fact that all UCD radio surveys to date require local magnetic field strengths above 1.6 kG, due to the high-frequency cut-off characteristic of ECMI generated emission. The capability of LOFAR to access the MHz frequency domain allows us to target objects with magnetic field strengths of tens of gauss. To establish the feasibility of using LOFAR to study the auroral environment of cool brown

Table 1. Summary of properties for our targets. Refs: 'e' indicates a rough estimate based on spectral type for $T_{\rm eff}$ and assuming an age range of 1–10 Gyr for the adopted mass. Otherwise, number indicates literature values taken from (1) Artigau et al. (2006); (2) Kirkpatrick et al. (2011); (3) Marsh et al. (2013); (4) Tannock et al. (in preparation); (5) Dupuy & Kraus (2013).

Target	Spectral type	D (pc)	$P_{\rm rot}$ (h)	Mass ($M_{\rm Jupiter}$)	$T_{\rm eff}$ (K)	Refs
SIMP 0136	T2.5	6.4 ± 0.3	2.5	40–70	1300 ± 200	1,1,1,e,e
WISE 1506	T6	$3.4^{+0.7}_{-0.4}$	1.74	30–60	1000 ± 200	2,3,4,e,e
WISE 1741	T9	$5.6^{+0.5}_{-0.4}$	–	10–35	620 ± 60	2,5,–,5,5

dwarfs with sub-kG fields, we have conducted a mini-survey of nearby brown dwarfs.

2 TARGET SELECTION

We selected three targets for deep LOFAR imaging based on proximity to the Solar system, and (where available) short rotation period. The aim was not to create an unbiased survey, but to select targets which maximized the chances of detecting low-frequency emission in the Nichols et al. (2012) model. We targeted three nearby brown dwarfs comprising one early-T dwarf: SIMP J013656.5+093347 (hereafter SIMP 0136; Artigau et al. 2006), and two late-T dwarfs: WISEPC J150649.97+702736.0, (hereafter WISE 1506; Kirkpatrick et al. 2011) and WISEPA J174124.26+255319.5 (hereafter WISE 1741; Gelino et al. 2011; Kirkpatrick et al. 2011; Scholz et al. 2011). Our target properties are summarized in Table 1.

It should be noted that SIMP 0136 was recently studied in detail by Apai et al. (2013) who used time-resolved spectroscopy to map the surface of the brown dwarf. SIMP 0136 appears to be variable on its rotational time-scale which has been attributed to a patchy atmosphere, with the surface covered by two distinct regions consisting of low-temperature thick clouds, and higher temperature, thin, bright clouds. Following the results of Hallinan et al. (2015) linking photometric variability and radio emission to aurorae, Kao et al. (2016) performed a survey targeting UCDs with known optical/near-IR variability. They detected at least one circularly polarized radio pulse from SIMP 0136 in the 4–8 GHz regime, as well as quiescent emission, and determined the surface B field strength to be a minimum of 2.5 kG. Neither of the other two targets have been detected in the radio.

We also note that since our targets were observed, SIMP 0136 and WISE 1506 were observed as part of the Pineda et al. (2016) brown dwarf Hα survey, and neither showed Hα emission, with limits of $f_\alpha < 4.9 \times 10^{-18}$ erg s^{-1} cm^{-2} and $f_\alpha < 5.8 \times 10^{-18}$ erg s^{-1} cm^{-2} reported respectively.

In addition, WISE 1506 was monitored photometrically with *Spitzer* as part of GO programme 11174 (PI: S. Metchev) to seek cloud-induced variability in a second phase of the Weather on Other Worlds survey (Metchev et al. 2015). WISE 1506 shows periodic variability in these observations with a period of 1.74 h (Tannock et al., in preparation).

3 OBSERVATIONS AND IMAGE CONSTRUCTION

We observed the targets in the frequency range between 111 and 169 MHz at 64 channels per sub-band in 8-bit mode using the HBA_DUAL_INNER configuration, with a standard integration time of 1 s. The integration time and frequency binning were designed to facilitate radio-frequency interference (RFI) removal. Each target was observed for a total of approximately 8 h, but because of the low declination of SIMP 0136 the observing time was broken up into two observations on two consecutive days (see Table 2 for details). In addition to providing the obvious benefit of a long integration, the observation duration was chosen to ensure that at least one rotation period was observed for all targets. In each case, the observations of the target field were preceded and followed by short, 10 min observations of flux calibrator sources.

After observation, the data were averaged by the observatory to four channels per sub-band (an HBA sub-band has a bandwidth of 200 kHz) and a 5 s integration time. No 'demixing' of bright off-axis sources was carried out by the observatory – this was deemed unnecessary given the sky positions of bright objects like Cygnus A and Cas A – and all further processing was carried out by us using the University of Hertfordshire high-performance computing facility.

The data were processed using the 'facet calibration' techniques which are described in detail by van Weeren et al. (2016, hereafter vW16) and Williams et al. (2016), with the preliminary processing implemented by us on the Hertfordshire system as described by Hardcastle et al. 2016, hereafter H16). Here we provide only a very brief overview of the data processing, and the reader is referred to vW16 and H16 for more details. After flagging for RFI and correcting for the effects of remote station clock offsets, the data were combined into 'bands' of 10 sub-bands each (with a total bandwidth of just under 2 MHz) and averaged again for computational speed to a 10 s integration time and 20 channels per band. As noted by H16, these parameters result in bandwidth and time-averaging smearing that affect peak flux densities at the ∼10 per cent level in full-resolution imaging at 2–3 deg from the pointing centre, but our aim in imaging the full LOFAR field of view for this project is simply to obtain the best possible sensitivity at the pointing centre; the averaging applied has no effect in the vicinity of our brown dwarf targets. The data were then phase self-calibrated using a model

Table 2. Observational details for the three targets.

Target	Start date	Start time	End date	End time	Time on source (h)
WISE 1506	2014-07-24	16:16:00	2014-07-25	00:16:00	8.00
SIMP 0136 (1)	2014-08-17	01:16:00	2014-08-17	05:01:09	3.75
SIMP 0136 (2)	2014-08-18	01:16:00	2014-08-18	05:01:09	3.75
WISE 1741	2014-10-01	13:16:00	2014-10-01	21:16:00	8.00

Table 3. Spectral windows, frequencies and LOFAR band/sub-band numbers used in facet calibration.

Spectral window	Frequency range (MHz)	Band numbers	Sub-band numbers
1	111–122	0–5	0–59
2	122–134	6–11	60–119
3	134–146	12–17	120–179
4	146–157	18–23	180–239
5	158–169	24–29	240–299

derived from combining the NRAO VLA Sky Survey (NVSS) with the LOFAR 150 MHz image to give initial phase solutions, and this provided phase solutions good enough to allow imaging of each band and subtraction of all the detected sources, giving the blank (residual) images and sky models needed for the facet calibration process.

Our facet calibration process differs from that described by vW16 in that we did not use the whole LOFAR bandwidth for the fitting, but instead divided the source into five spectral windows each consisting of six 2 MHz bands. As discussed by H16, this process has both advantages and disadvantages when compared to the vW16 approach. The advantages are (i) that each spectral window can be calibrated in parallel, speeding up the process considerably; (ii) that flux scale corrections can be derived as a function of frequency rather than across the whole LOFAR band, as described below; and (iii) that we can measure flux density across the band, potentially allowing the measurement of in-band spectral index. The disadvantages are that there is less signal-to-noise for the self-calibration required in the facet calibration process, potentially making the results less good, that phase offsets may be introduced between the different data sets, and that since the resulting images must be combined in the image plane, requiring us to convolve all images to the same resolution before summing them, the image resolution is limited to the resolution of the lowest frequency LOFAR band. In the present case, we required good flux calibration and wished to be able to constrain the source spectrum in the event of a BD detection, so we considered the advantages to outweigh the disadvantages. Accordingly, we used the five spectral windows listed in Table 3, giving a total of about 60 MHz of bandwidth. The upper end of the HBA bandwidth is badly affected by RFI and was not used.

The facet calibration process was run on these five spectral windows, imaging the whole $\sim$30 deg^2 LOFAR field of view. This gives us for each target five large (approx 20 000 $\times$ 20 000 1.5-arcsec pixels) images, one for each spectral window (we combined the two observations of SIMP 0136 in the image plane at this point). The images at each frequency band were convolved to matching resolution and a primary beam correction was applied in the image plane.

Finally, we had to correct the flux scale for these images to remove the frequency-dependent effects of the fact that transfer of the gains from the flux calibrator does not take full account of the effect on the beam of the different elevations of calibrator and target source. We did this (see H16 for more details) by extracting a multi-frequency source catalogue for each image using PYBDSM, cross-matching with the Very Large Array Low-frequency Sky Survey Redux (VLSSr; Lane et al. 2014) and NVSS surveys to produce a small sample of $\sim$50 bright sources detected in all bands, and determining the scaling factors for each spectral window that produced the best power-law fits to the spectra of all sources in the source catalogue after outlier rejection. Total LOFAR flux densities are used in this process, so it is unaffected by bandwidth or time-averaging smearing at large distances from the pointing centre; only sources that have deconvolved angular sizes less than 20 arcsec in the LOFAR images, and are thus unresolved in NVSS and VLSS images, are used to avoid any effects due to the mismatch in LOFAR and NVSS/VLSS resolutions. With these correction factors applied, the flux densities we measure should be correct on the scale of Scaife & Heald (2012), since both VLSSr and NVSS are on this scale. A caveat is that there may well be some spectral curvature between the LOFAR and NVSS frequencies, which would tend to cause us to underestimate the magnitude of the flux scale correction, particularly at the high-frequency end of the LOFAR band. While this is probably a real effect, it can only be overcome if a lower frequency survey than NVSS is available, which is not the case for all of our fields. We chose to use NVSS for all three fields for consistency. The nominal statistical error on the correction factors is of the order of 1 per cent, but systematic effects, including that of spectral curvature, are probably larger; the limiting factor is probably the VLSSr absolute calibration, which we estimate to be good to $\sim$10 per cent based on the discussion by Lane et al. (2014). For the purposes of this paper, 10 per cent flux density uncertainties are acceptable.

With the correction factors applied, we combined the images for the five spectral windows to produce a single image at a nominal frequency of 140 MHz, with a total bandwidth of 58 MHz.

4 RESULTS

Images of the fields around the brown dwarfs are presented in Appendix A.

The typical central rms noise in our 140 MHz images is a little over 200 μJy beam^{-1}. This is about a factor of 2 worse than the best fields of vW16 and H16. We consider this to be the result of a combination of factors. Facet calibration worked well in the SIMP 0136 field, but on the equator the sensitivity of LOFAR is necessarily lower because of projection effects. The WISE 1506 field contains two very bright sources, 3C 309.1 and 3C 314.1, and it is challenging to remove these completely even with facet calibration, leading to a higher level of noise. And WISE 1741 lies close to a bright ($\sim$0.8 Jy), very extended (11 arcmin) extragalactic source with complex structure which we were unable to deal with well in facet calibration, increasing the noise in the facet containing the target.

No sources are visible at (or near) the locations of any of the brown dwarf targets. We estimate the following 3σ detection limits for our targets integrated across the full 111–169 MHz frequency range: WISE 1506: $<$0.72 mJy; WISE 1741: $<$0.87 mJy; SIMP 0136: $<$0.66 mJy.

5 DISCUSSION

A key aim of these observations was to assess whether the low detection rate of brown dwarfs at GHz frequencies was due to local magnetic field strengths being sufficiently low to restrict ECMI emission to the 100 MHz frequency regime. Our lack of detection for any of our targets does not provide a basis for a strong conclusion in this matter.

We note that SIMP 0136 has been detected by Kao et al. (2016) with a pulse spectral flux density of 0.23 mJy at 4–8 GHz. Assuming a flat spectrum, this would place this target below our detection limits. This implies that the radio luminosity of this object does not increase significantly with decreasing frequency. The GHz observations of SIMP 0136 by Kao et al. (2016) reached a depth $\sim$100 times fainter than our LOFAR observations, and it is reasonable to infer

Table 4. Adopted parameters for our UCDs and resulting Pedersen conductance estimates. Please see caveats in Section 5.

Target	B_i (kG)	$P_{\rm rot}$ (h)	Σ_P (mho)
SIMP 0136	2.5	2.5	<0.3
WISE 1506	0.7	1.74	<0.1
WISE 1741	0.3	2	<0.5

that an increase in sensitivity at this level will be required to robustly test for a higher detection fraction at low frequency. Moreover, such sensitive observations of GHz detected objects could also set useful constraints on the location of the field-aligned voltage driving the currents. For example, if it is located at an altitude less than ∼2.5 stellar radii up the dipolar field lines, then no emission would be expected at LOFAR frequencies.

The GHz detection of SIMP 0136 tells us that the electrodynamic engine that drives the radio emission is present in this case, and we are thus able to derive useful information from our upper limits on the low-frequency flux density in light of this fact. However, in the other two cases, any further interpretation of our results relies on the assumption that the presumed electrodynamic engine is present. Since the nature of the electrodynamic engine for the auroral emissions in brown dwarfs is not determined, this is highly speculative and the following discussion in respect of these two targets must be considered accordingly.

By considering the theoretical framework outlined by Nichols et al. (2012), we now use the upper limits to the spectral flux densities derived here to estimate upper limits of the Pedersen conductance of these bodies, and again highlight the caveats discussed in the previous paragraph. We employ the fiducial parameters considered by Nichols et al. (2012), i.e. angular velocities which transition from 25 per cent to full corotation over the space of ∼1° centred on 15° co-latitude, as shown in their fig. 1a, and values for the high-latitude electron population temperature and number density of 2.5 keV and 0.01 cm^{-3}, respectively, i.e. Jovian values. We recognize that these parameters are unknown at brown dwarfs, and thus may differ considerably to these figures but in the absence of data to the contrary, the Jovian figures enable a reasonable initial impression as to what conductances might be expected (note that the expected power variation in respect of these quantities is shown in fig. 2 of Nichols et al. 2012).

In addition to assuming a Jovian-like plasma environment, we adopt the lower limit estimated by Kao et al. (2016) of 2.5 kG as our polar magnetospheric magnetic field strength, B_i, for SIMP 0136. For the other two targets, we estimate their polar magnetic field strengths following Reiners & Christensen (2010). For WISE 1741, we adopt a rotation period at the lower end of the so far observed $P_{\rm rot}$ distribution of brown dwarfs (e.g. Metchev et al. 2015) since we are seeking an upper limit on the Pedersen conductance.

Employing these parameter values, along with those indicated in Table 4, and assuming that the radio is beamed into the canonical 1.6 sr yield upper limits for the Pedersen conductances of the order of a tenth of a mho in each case, i.e. consistent with the lower end of Jovian estimates, which range from ∼0.1 mho to ∼10 mho (e.g. Strobel & Atreya 1983; Bunce & Cowley 2001).

6 CONCLUSIONS

We have performed a limited search for low-frequency radio emission from some of the nearest rapidly rotating brown dwarfs to the Sun. We did not detect any of them, and estimate the following 3σ detection limits for our targets integrated across the full 111–169 MHz frequency range: WISE 1506: <0.72 mJy; WISE 1741: <0.87 mJy; SIMP 0136: <0.66 mJy. These limits are consistent with these objects displaying ionospheric Pedersen conductances of similar magnitude to those found in the Jovian environment or lower. WISE 1506, in particular, is at the lower extreme of the Jovian scenario.

The significant observational time required to achieve these limits suggests that any systematic low-frequency radio study of the auroral environment of substellar neighbours will require substantial dedication of currently available resources, or an improvement in the low-frequency capability not currently foreseen in upcoming facilities such as the Square Kilometre Array.

ACKNOWLEDGEMENTS

BB acknowledges financial support from the European Commission in the form of a Marie Curie International Outgoing Fellowship (PIOF-GA-2013- 629435). MJH and WLW acknowledge support from the UK's Science and Technology Facilities Council [grant number ST/M001008/1]. SLC is supported by the College of Science and Engineering at the University of Leicester. SPL acknowledges support from the UK's Science and Technology Facilities Council [grant number ST/M001350/1].

REFERENCES

Antonova A., Hallinan G., Doyle J. G., Yu S., Kuznetsov A., Metodieva Y., Golden A., Cruz K. L., 2013, A&A, 549, A131
Apai D., Radigan J., Buenzli E., Burrows A., Reid I. N., Jayawardhana R., 2013, ApJ, 768, 121
Artigau É., Doyon R., Lafrenière D., Nadeau D., Robert J., Albert L., 2006, ApJ, 651, L57
Benz A. O., Guedel M., 1994, A&A, 285, 621
Berger E., 2002, ApJ, 572, 503
Berger E., 2006, ApJ, 648, 629
Berger E. et al., 2001, Nature, 410, 338
Berger E. et al., 2009, ApJ, 695, 310
Bunce E. J., Cowley S. W. H., 2001, Planet. Space Sci., 49, 1089
Burgasser A. J., Geballe T. R., Leggett S. K., Kirkpatrick J. D., Golimowski D. A., 2006, ApJ, 637, 1067
Burgasser A. J. et al., 2010, ApJ, 725, 1405
Burningham B. et al., 2011, MNRAS, 414, 3590
Canty J. I. et al., 2015, MNRAS, 450, 454
Cowley S. W. H., Bunce E. J., 2001, Planet. Space Sci., 49, 1067
Cushing M. C. et al., 2011, ApJ, 743, 50
Delorme P. et al., 2013, A&A, 553, L5
Dupuy T. J., Kraus A. L., 2013, Science, 341, 1492
Faherty J. K., Rice E. L., Cruz K. L., Mamajek E. E., Núñez A., 2013, AJ, 145, 2
Gelino C. R. et al., 2011, AJ, 142, 57
Gizis J. E., Monet D. G., Reid I. N., Kirkpatrick J. D., Liebert J., Williams R. J., 2000, AJ, 120, 1085
Grodent D., Clarke J. T., Kim J., Waite J. H., Cowley S. W. H., 2003, J. Geophys. Res., 108, 1389
Gudel M., Schmitt J. H. M. M., Bookbinder J. A., Fleming T. A., 1993, ApJ, 415, 236
Hallinan G., Antonova A., Doyle J. G., Bourke S., Brisken W. F., Golden A., 2006, ApJ, 653, 690
Hallinan G. et al., 2007, ApJ, 663, L25
Hallinan G., Antonova A., Doyle J. G., Bourke S., Lane C., Golden A., 2008, ApJ, 684, 644
Hallinan G. et al., 2015, Nature, 523, 568
Hill T. W., 1979, J. Geophys. Res., 84, 6554
Hardcastle M. J. et al., 2016, MNRAS, 462, 1910 (H16)
Isbell J., Dessler A. J., Waite J. H., Jr, 1984, J. Geophys. Res., 89, 10716

Jaeger T. R., Osten R. A., Lazio T. J., Kassim N., Mutel R. L., 2011, AJ, 142, 189
Kao M. M., Hallinan G., Pineda J. S., Escala I., Burgasser A., Bourke S., Stevenson D., 2016, ApJ, 818, 24
Kirkpatrick J. D. et al., 1999, ApJ, 519, 802
Kirkpatrick J. D. et al., 2011, ApJS, 197, 19
Lane W. M., Cotton W. D., van Velzen S., Clarke T. E., Kassim N. E., Helmboldt J. F., Lazio T. J. W., Cohen A. S., 2014, MNRAS, 440, 327
Line M. R., Teske J., Burningham B., Fortney J., Marley M., 2015, ApJ, 807, 183
Liu M. C. et al., 2013, ApJ, 777, L20
Lynch C., Murphy T., Ravi V., Hobbs G., Lo K., Ward C., 2016, MNRAS, 457, 1224
McLean M., Berger E., Reiners A., 2012, ApJ, 746, 23
Marsh K. A., Wright E. L., Kirkpatrick J. D., Gelino C. R., Cushing M. C., Griffith R. L., Skrutskie M. F., Eisenhardt P. R., 2013, ApJ, 762, 119
Metchev S. A. et al., 2015, ApJ, 799, 154
Mohanty S., Basri G., Shu F., Allard F., Chabrier G., 2002, ApJ, 571, 469
Naud M.-E. et al., 2014, ApJ, 787, 5
Nichols J. D., Cowley S. W. H., 2003, Ann. Geophys., 21, 1419
Nichols J., Cowley S., 2004, Ann. Geophys., 22, 1799
Nichols J. D., Cowley S. W. H., 2005, Ann. Geophys., 23, 799
Nichols J. D., Burleigh M. R., Casewell S. L., Cowley S. W. H., Wynn G. A., Clarke J. T., West A. A., 2012, ApJ, 760, 59
Pineda J. S., Hallinan G., Kirkpatrick J. D., Cotter G., Kao M. M., Mooley K., 2016, ApJ, 826, 73
Ravi V., Hallinan G., Hobbs G., Champion D. J., 2011, ApJ, 735, L2
Reiners A., Christensen U. R., 2010, A&A, 522, A13
Route M., Wolszczan A., 2012, ApJ, 747, L22
Route M., Wolszczan A., 2013, ApJ, 773, 18
Scaife A. M. M., Heald G. H., 2012, MNRAS, 423, L30
Scholz R.-D., Bihain G., Schnurr O., Storm J., 2011, A&A, 532, L5
Strobel D. F., Atreya S. K., 1983, in Dessler A. J., ed., Ionosphere. Cambridge Univ. Press, Cambridge UK, p. 51
Treumann R. A., 2006, A&AR, 13, 229
van Weeren R. J. et al., 2016, ApJS, 223, 2 (vW16)
Williams P. K. G., Berger E., Zauderer B. A., 2013, ApJ, 767, L30
Williams P. K. G., Cook B. A., Berger E., 2014, ApJ, 785, 9
Williams P. K. G., Casewell S. L., Stark C. R., Littlefair S. P., Helling C., Berger E., 2015, ApJ, 815, 64
Williams W. L. et al., 2016, MNRAS, 460, 2385
Zarka P., 1998, J. Geophys. Res., 103, 20159

APPENDIX A: IMAGES

Here we show LOFAR images of the fields around the brown dwarfs. These 1000 × 1000 arcsec images are a small fraction of the total field of view imaged by LOFAR.

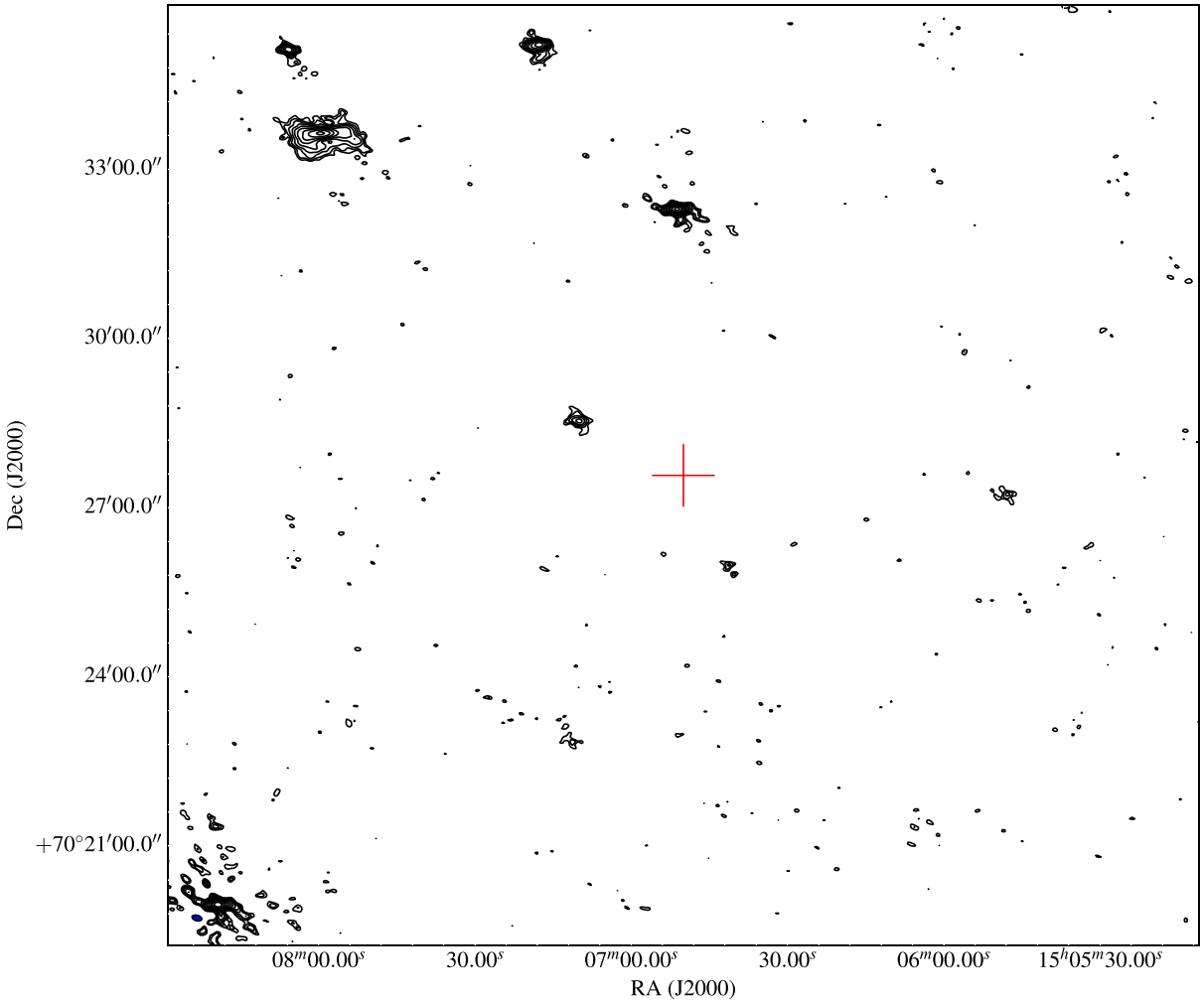

Figure A1. The field around WISE 1506. A red cross marks the position of the target. rms noise at this position is 240 μJy beam^{-1}; contours are at $3 \times 240 \times (1, \sqrt{2}, 2, \ldots)$ μJy beam. The resolution of the image is 9.3 × 5.5 arcsec, shown by a blue ellipse in the bottom-left corner.

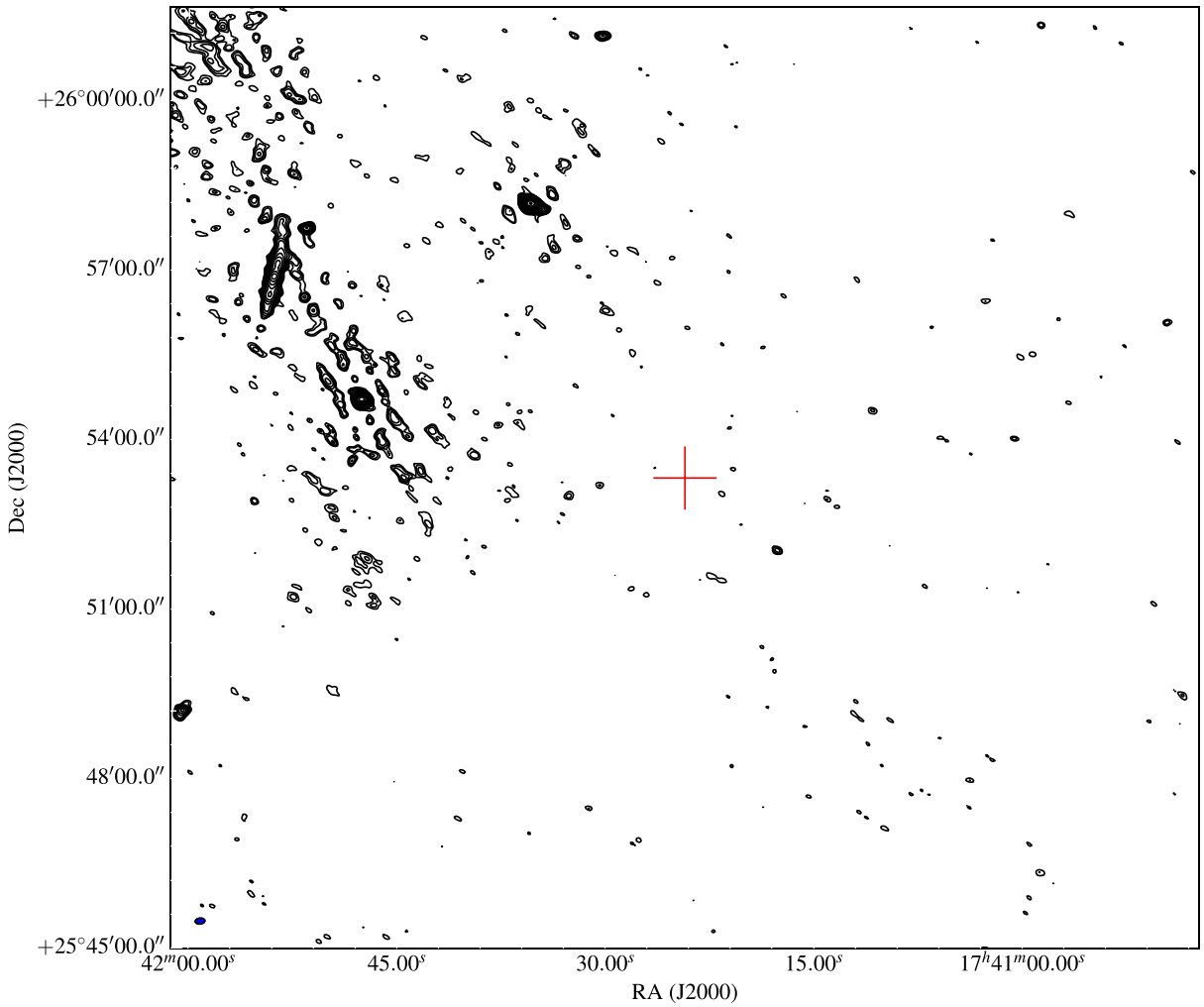

Figure A2. The field around WISE 1741. As Fig. A1, but the rms noise at this position is 290 μJy beam^{-1} and the resolution 9.4 × 6.3 arcsec. The extended source referred to in the text can be seen to the NE.

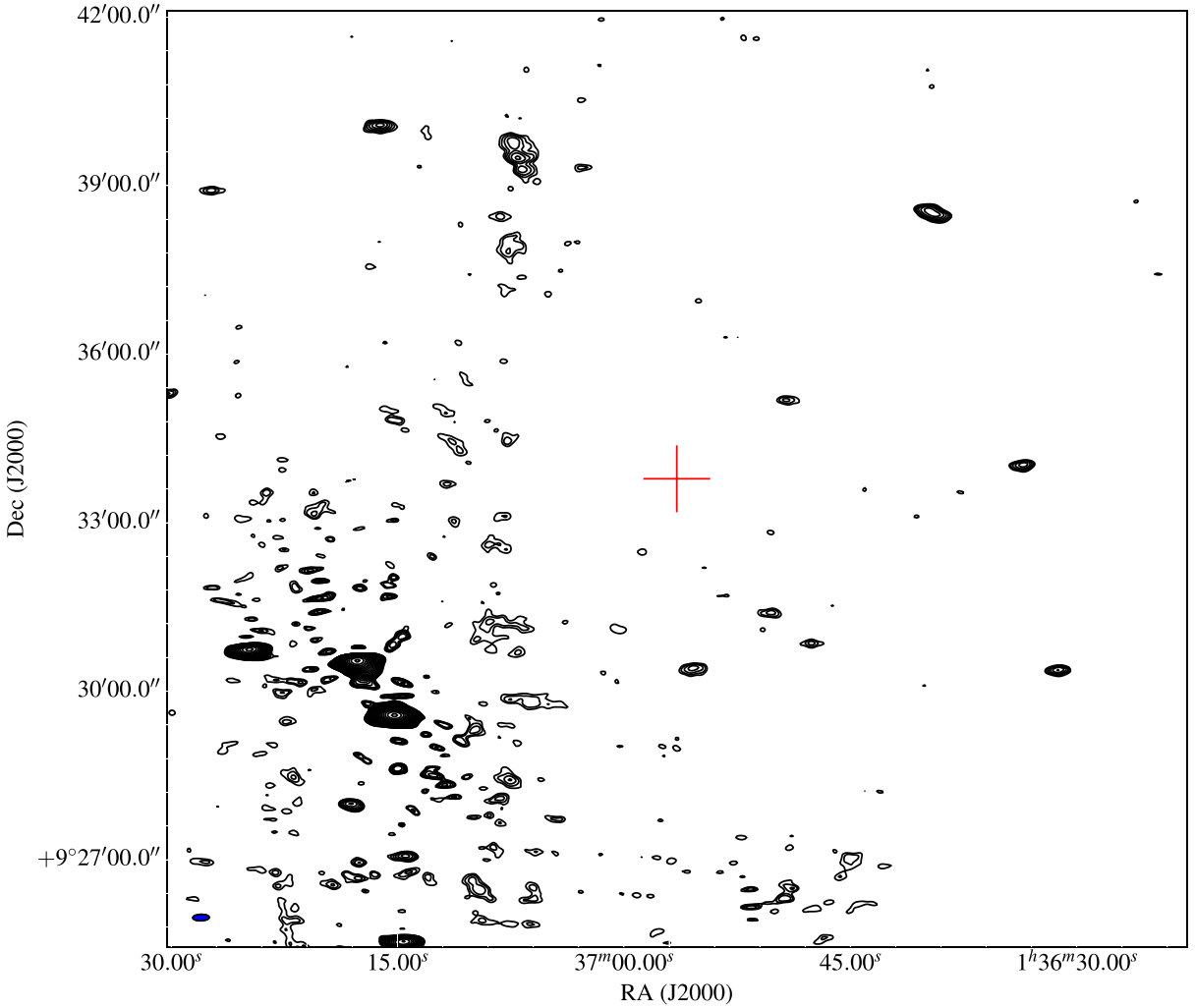

Figure A3. The field around SIMP 0136. As Fig. A1, but the rms noise at this position is 220 μJy beam^{-1} and the resolution 16.1 × 6.7 arcsec. In the SE of the image, dynamic range limitation around the bright source 4C +09.06 (4.7 Jy) can be seen.

This paper has been typeset from a TEX/LATEX file prepared by the author.